Electrochimica Acta 194 (2016) 317–329

Contents lists available at ScienceDirect

Electrochimica Acta

journal homepage: www.elsevier.com/locate/electacta

Effects of Operating Temperature on the Electrical Performance of a Li-air Battery operated with Ionic Liquid Electrolyte

Kisoo Yoo, Aniruddha M. Dive, Saeed Kazemiabnavi, Soumik Banerjee, Prashanta Dutta*

School of Mechanical and Materials Engineering, Washington State University, Pullman, Washington 99164-2920, USA

ARTICLE INFO

Article history:
Received 10 November 2015
Received in revised form 22 January 2016
Accepted 16 February 2016
Available online 20 February 2016

Keywords:
lithium-air battery
ionic liquid electrolyte
specific capacity
cell performance

ABSTRACT

Li-air cell operated with ionic liquid electrolytes is a very promising energy storage technology for electric vehicle and plug-in hybrid electric vehicle due to several favorable characteristics of ionic liquids. However, Li-air cells that employ room temperature ionic liquid (RTIL) electrolytes exhibit poor performance due to limited oxygen solubility and low reactant species mobility. To circumvent these aforementioned drawbacks, we investigated the electrical performance of a Li-air cell with ionic liquid electrolytes operating at high temperature. A continuum based model is used to quantify the performance of the Li-air cell, with an ionic liquid (MPPY-TFSI) electrolyte, as a function of operating temperature. Simulations at the atomistic scale, such as molecular dynamics (MD) and density functional theory (DFT) calculations are used to obtain key properties for the continuum model. These properties include electron transfer reaction rate constant, species diffusivity and oxygen solubility. The MD simulations indicate that oxygen solubility in ionic liquid increases with temperature, which is very favorable for high temperature operation. The continuum based cell level simulation results show that the battery performance can be improved significantly by increasing operating temperature. For instance, specific capacity as high as 3000 mAh/g can be achieved at 110 °C operating temperature, which is almost 25 times higher than its counterpart at room temperature. Simulation results also reveal that by increasing the operating temperature, the specific capacity can be improved significantly for high load current density, which is one of the most critical drawbacks in RTIL based Li-air battery. We also studied the effect of cathode thickness on the performance of Li-air battery at different operating temperatures. The transport limitation of oxygen and lithium ions can be alleviated at higher operating temperatures, suggesting that even thicker cathode materials can be used to enhance the cell capacity at elevated temperature.

1. Introduction

Even though recent developments in Li-ion battery have revolutionized the portable electronics market, it still falls short of meeting the demands of the automobile industry for electric vehicles and hybrid electric vehicles. For instance, the current driving range of most Li-ion based electric vehicles is limited to 200 km, which is practically useless for any long distance trip [1]. The successful development of electric vehicles requires breakthrough in battery technology that leads to very high specific capacity as well as cell capacity at reasonable price. The Li-air battery, which has a theoretical energy density comparable to that of gasoline [2], has the potential to meet the demand of auto industry and supply power for longer driving range. As a matter of fact, the specific energy of lithium-air battery can be 10 times as high as that of lithium-ion battery. This high specific energy can be attributed to a light cathode employed in Li-air battery, where the principal reactant (oxygen) is taken directly from atmosphere rather than stored in heavy cathode materials, such as $LiMn_2O_4$, $LiFePO_4$, and $LiCoO_2$ [3]. The superior performance of Li-air battery has been reported in recent studies where organic solvent was used as electrolytes [4,5]. However, the cyclic performance of those batteries was very low since lithium carbonate is produced from organic electrolytes during discharge [6]. Owing to the very high chemical stability of lithium carbonate, high electric potential is required to recover lithium ions from lithium carbonate during charging process. This high charging potential can oxidize the electrolyte, which results in the degradation of electrolytes as well as formation of insulation layer on the electrode surface [7]. Another major drawback of widely used

* Corresponding author: Tel.: +1 509 335 7989; fax: +1 509 335 4662.
E-mail address: prashanta@wsu.edu (P. Dutta).

http://dx.doi.org/10.1016/j.electacta.2016.02.099
0013-4686/

organic electrolytes is flammability due to their characteristic high vapor pressure. The flammability of these electrolytes can lead to major safety hazard, especially in the Li-air battery due to its open form architecture.

To overcome aforementioned drawbacks, ionic liquids have been used as electrolytes in lithium-air batteries [8]. Ionic liquids have low vapor pressure and they are chemically and thermally stable solvents. However, the performance of RTIL based Li-air battery was inferior compared to that of organic electrolytes because of high viscosity and low diffusivity at room temperature. Moreover, the oxygen solubility and diffusivity are much lower in ionic liquid electrolytes compared to organic liquids, which severely affect the electrical performance of Li-air battery [9]. Furthermore, lithium ion mobility is limited in ionic liquids because of the formation of charged clusters between lithium ion and ionic liquid anions [10]. However, in a recent work, Deshpande et al. [10] have shown that diffusivities of lithium ions increase with temperature in ionic liquid electrolytes, which can improve the lithium ion mobility. As a matter of fact, Kuboki et al. [8] have demonstrated the feasibility of high temperature (over 80 °C) operation of Li-air battery using ionic liquid electrolyte. While higher specific capacity was obtained at elevated temperature, the battery was tested at very low current density conditions ~0.1 A/m^2, which is not suitable for most applications. In this work, the performance of Li-air batteries with ionic liquid electrolytes is studied at high temperatures since species transport properties, such as diffusivity and mobility, of the electrolytes could be improved at higher operating temperatures. Here, MD and DFT calculations are performed to calculate properties of ionic liquids and reaction constants, and continuum level analysis is carried out to predict the battery performance at different load current densities. Furthermore, the effects of varying cathode thickness are studied to demonstrate the species transport behavior in ionic liquid electrolytes and its consequence on cell performance at different working temperatures.

2. Model

2.1. Model System

A typical Li-air cell consists of lithium anode, porous separator and catalyst loaded porous carbon cathode as shown in Fig. 1. Here, porous cathode and separator are filled with electrolyte, which provides route for lithium ion and oxygen transportation. Typically, solid lithium foil is used as anode material since it can decrease the anode weight by eliminating structural materials (e.g. graphite), and anodic reaction takes place only at the interface between lithium foil and electrolyte. On the other hand, cathodic reaction occurs in the entire porous cathode surface. During the discharge state, lithium metal is oxidized and dissolved into electrolyte continuously by releasing an electron as

$$Li \rightarrow Li^+ + e^- \quad (1)$$

The electron released from lithium metal moves to cathode side through outer loop while lithium ions pass through the electrolyte to cathode region. The lithium ion is subsequently reduced at the cathode side (Fig. 1) in presence of electron and oxygen derived from atmospheric air through the gas diffusion layer (GDL) as [11]

$$O_2 + e^- \rightarrow O_2^- \quad (2)$$

$$O_2^- + Li^+ \rightarrow LiO_2 \quad (3)$$

$$2LiO_2 \rightarrow Li_2O_2 + O_2 \quad (4)$$

Thus, the overall reaction for a Li-air battery can be represented as

$$2Li + O_2 \rightarrow Li_2O_2 \quad (5)$$

During the charge process, the anodic and cathodic reactions are reversed. In other words, lithium peroxide is oxidized at the

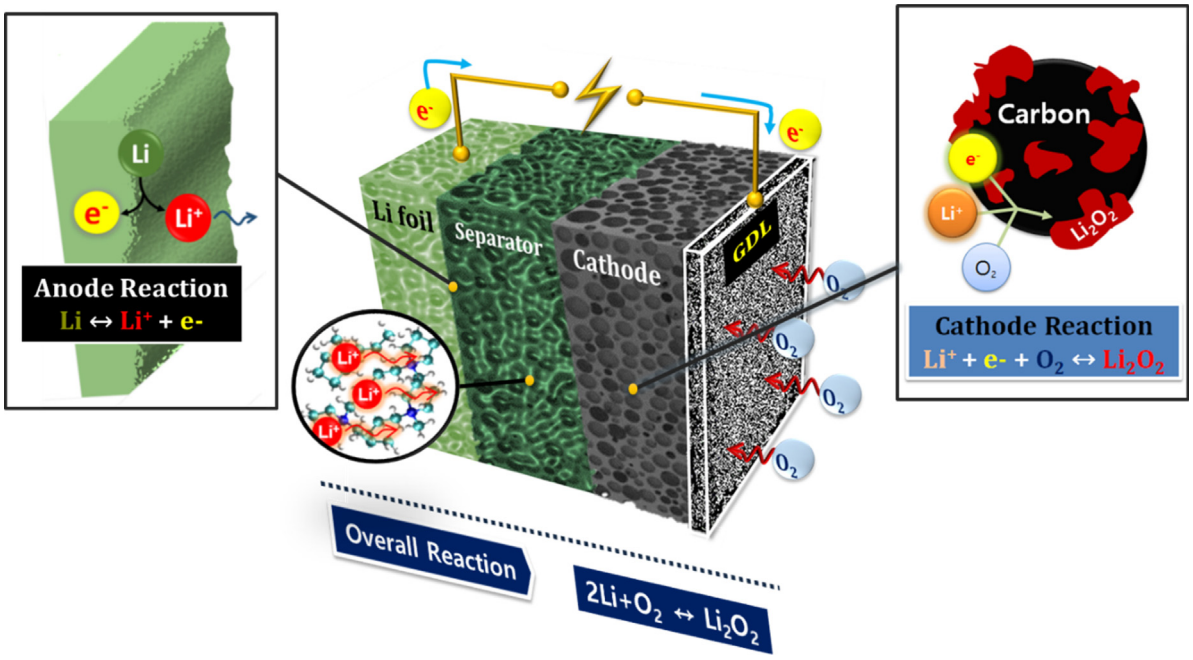

Fig. 1. Schematic illustration of Li-air battery with corresponding electrochemical reactions at anode and cathode side is provided. Li ion dissolves into electrolyte due to oxidation at anode while it reduces with oxygen at cathode during discharge stage. Oxygen is introduced continuously to the cell through the air-breathing cathode.

porous cathode side to form lithium ion and oxygen. The reaction product oxygen is released to atmospheric air, while the other reaction product, lithium ion, returns to the anodic side through electrolyte. The lithium ion is finally reduced to lithium in presence of the charge current, and recovered on the lithium foil. In this study, a mixture of lithium salt (Li-TFSI) and an ionic liquid (MPPY-TFSI) solvent is used as model electrolyte.

2.2. Mathematical Model for Li-air Cell

2.2.1. Chemical Kinetics

In a Li-air cell, the reaction rates at the anode and cathode sides are formulated with surface overpotential as well as concentration of reaction species such as lithium ion (C_{Li}^{+}) and oxygen (C_{O2}) described later. The local transfer current density at the reaction sites can be calculated using the Butler-Volmer Equation [12]. However, in this study, the reaction rates are formulated from Tafel equations, since the electrical performances are only considered for discharge process [13].

$$\text{Anode}: \quad j_a = i_0 \exp\left(\frac{\beta n F}{RT}\eta_a\right) \tag{6a}$$

$$\text{Cathode}: \quad j_c = -F k_c C_{Li^+}^2 C_{O_2} \exp\left[-\frac{(1-\beta)nF}{RT}\eta_c\right] \tag{6b}$$

where n, R, T, β, F, k_c, and i_0 are number of electrons involved in electrode reaction, gas constant, temperature, symmetric coefficient, Faraday constant, cathode reaction constant and exchange current density, respectively. The surface over-potential (η) is expressed as

$$\eta_i = \phi_s - \phi_l - E_i \tag{7}$$

where ϕ_s, ϕ_l and E are solid and liquid phase electric potential and open circuit potential, respectively. The subscript i becomes "c" for cathode and "a" for anode.

2.2.2. Transport Equations

The transport equations for Li-air battery with organic liquid electrolytes was introduced recently [14,15]. But these models cannot be applied to the Li-air battery operated with ionic liquid electrolytes. Unlike organic electrolytes, ionic liquid electrolytes consist of three ionic species. For instance, the ionic electrolyte considered in this study contains two cations (Li^+, $MPPY^+$) and one anion ($TFSI^-$) Thus, models commonly used for binary electrolytes are not useful for ionic liquid based ternary systems. In a recent study, we developed a mathematical model for ionic liquid based ternary electrolyte system to study lithium-ion battery. Here, we have modified those transport equations for Li-air battery [16].

In a Li-air cell, both lithium ion and oxygen can be transported to porous separator and the cathode region through electrolyte. Owing to the very low concentration of oxygen in the ionic liquid electrolyte, the oxygen concentration in the porous media can be obtained from the simple diffusion transport using Bruggeman correlation [17] as

$$\frac{\partial(\varepsilon C_{O_2})}{\partial t} = \nabla \cdot \left(\varepsilon^{1.5} D_{O_2} \nabla C_{O_2}\right) + S_{O_2} \tag{8}$$

where ε is porosity of the material (either separator or cathode) and D_{O_2} is the oxygen diffusivity. It is important to note that the applicability of the Bruggeman correlation is only valid for isotropic porous media [18]. In other words, the simplified Bruggeman correlation cannot capture particle polydispersity and electrode inhomogeneity into species transport phenomena [19].

The source (sink) term for oxygen are calculated from transfer current density and specific reaction surface area (a) as

$$S_{O_2} = \frac{a j_c}{nF} \tag{9}$$

But the mass transport equation for lithium ion needs to be derived from Maxwell-Stefan equations due to extremely high concentration of the ions in ionic liquid electrolyte. Following our earlier work [16], the Li ion concentration in ionic liquid electrolyte can be obtained in the porous material as

$$\frac{\partial(\varepsilon C_{Li^+})}{\partial t} - \nabla \cdot \left[\varepsilon^{1.5} \tilde{D}_{Li^+} \nabla C_{Li^+} + z \tilde{\omega}_{Li^+} \nabla \Phi_l (\varepsilon C_{Li^+})\right] = S_{Li^+} \tag{10}$$

Here $\tilde{D}_{Li^+}$ and $\tilde{\omega}_{Li^+}$ are apparent diffusivity and mobility for lithium ion in ionic liquid electrolyte, and these parameters can be obtained as

$$\tilde{D}_{Li^+} = \frac{2 D_{12} D_{23}}{D_{12} + D_{13} + 2(D_{23} - D_{13})\chi_1} \tag{11}$$

$$\tilde{\omega}_{Li^+} = \left(1 + \frac{D_{23}}{D_{12}}\right)\frac{\tilde{D}F}{RT} \tag{12}$$

where χ_i is the mole fraction and D_{ij} are Maxwell-Stefan diffusivities. The subscripts 1, 2 and 3 represent 1: Li^+, 2: $MPPY^+$ and 3: $TFSI^-$. Like oxygen transport equation, the source term for the lithium ion can be estimated from

$$S_{Li^+} = \frac{a j_c}{nF} \tag{13}$$

The mass conservation equation for lithium peroxide (Li_2O_2) can be obtained by balancing the transient term with the source tem as

$$\frac{d(C_{Li_2O_2})}{dt} = -\frac{a j_c}{nF} \tag{14}$$

Here the diffusion term is not considered since the Li_2O_2 is generally insoluble in the electrolyte. In a lithium-air battery, Li_2O_2 fills the cathode void area during the discharge state. Therefore, cathode porosity can be obtained by subtracting the space taken by Li_2O_2 from initial cathode porous area (ε^0) as

$$\varepsilon = \varepsilon^0 - C_{Li_2O_2} \cdot \frac{M_{Li_2O_2}}{\rho_{Li_2O_2}} \tag{15}$$

where $M_{Li_2O_2}$ and $\rho_{Li_2O_2}$ are molecular weight and the mass density of Li_2O_2, respectively.

The electric potential in a lithium-air cell can be divided into two parts: solid phase potential (ϕ_s) and liquid phase potential (ϕ_l). Solid phase potential is only pertinent to the solid regions of cathode materials, while the liquid phase potential is related to electrolyte, and exists throughout the computational domain. The former potential can be obtained from charge conservation in the cathodic solid as

$$\nabla \cdot \left[\sigma(1-\varepsilon)^{1.5} \nabla \phi_s\right] = a j_c \tag{16}$$

where σ is electrical conductivity, which is given as material property. Liquid phase electric potential equation is more intricate because of Li ion movement in concentrated solution. From charge conservation, liquid phase electric potential equation is derived as

$$\nabla \cdot (\lambda \varepsilon^{1.5} \nabla \phi_l) = -a j_c - \nabla \cdot \left[\frac{F(D_{13} - D_{23})}{D_{13}} \varepsilon^{1.5} \tilde{D} \nabla C_1\right] \tag{17}$$

Here, ionic conductivity (λ) is defined as

$$\lambda = C_T D_{23} z^2 F \left(\frac{D_{13}/D_{23} - 1}{D_{13}} \tilde{\omega} \chi_1 + \frac{F}{RT} \right) \quad (18)$$

where C_T is total molar concentration of electrolyte.

2.3. Assumptions

In this study, following assumptions were used to simplify the mathematical model.

- Maxwell-Stefan framework is applicable to describe mutual diffusion phenomena in ionic liquid systems.
- Lithium salt is fully ionized in the ionic liquid solvent and there is no neutral species in the electrolyte.
- Charge separation is impossible in electrolytic solutions, so, electroneutrality condition is maintained in ionic liquid electrolyte.
- Size of dendrite is small enough compared with simulation domain to neglect the effect of anode surface roughness.
- Temperature remains uniform throughout the cell.
- Lithium peroxide deposits homogeneously onto porous cathode region.

2.4. Boundary Conditions

The left boundary of the computational domain, shown in Fig. 1, is located at the interface of anode foil and the electrolyte, while the right boundary is positioned at the edge of the porous cathode and the gas diffusion layer (GDL). The boundary conditions for the mass and charge conservation equations are listed in Table 1. The mass flux of the lithium ion at the left boundary was formulated with anode current density while zero flux was applied at the right boundary. With regards to oxygen, constant concentration is prescribed at the right boundary but zero flux was applied at the left end. Here, the oxygen concentration is calculated from oxygen solubility and oxygen partial pressure at atmospheric conditions. For liquid phase electric potential, the electrically insulated condition was applied at the right boundary, while load current value was given at the left end of the domain since the current is induced by the dissolution of lithium ions at the reaction surface. On the other hand, for solid phase electric potential, insulation condition was applied at the left edge of cathode material, while load current value was given at the right side of the computational domain.

2.5. Numerical Method for Cell Level Analysis

In this study, discretized algebraic equations were obtained to solve nonlinear mass and charge conservation equations. For the spatial differencing, a finite volume method with power law scheme was used, while a first order-accurate implicit scheme was applied for the time differencing. Thomas algorithm was used to solve tri-diagonal system of the equations. Here, all equations had been solved simultaneously using sequential method with 10^{-5} convergence tolerance. An in-house code was developed based on C++ and numerical calculations were performed on an Intel Xeon 2.4 GHz CPU.

3. Chemical Properties

3.1. Reaction Rate Constant

In the present study, the electron transfer reaction rate constant for the electrochemical oxidation of lithium metal at anode was calculated using a novel method, based on Marcus's theory [20]. The effect of solvent is accounted for by using the Conductor-like Screening Model (COSMO) [21], which is an approach to model dielectric screening in solvents. In the framework of Marcus's theory, the determination of the electron transfer rate constant requires calculation of Gibbs free energies for all the species involved in the oxidation of pure lithium metal into positively charged lithium ions as well as the inner and outer sphere reorganization energies for the electron transfer in the presence of ionic liquid electrolyte, which was described implicitly using COSMO solvation model. DFT approach was used to calculate all free energies within the Becke, three-parameter, Lee–Yang–Parr (B3LYP) level of theory to account for exchange correlation effects. The details of the model were described in a prior work of Kazemiabnavi et al. [22,23], which investigated the effect of dielectric constant of the ionic liquid electrolyte on the kinetics and energetics of the electron transfer reaction at the anode-electrolyte interface. DFT based study shows that the magnitude of the driving force for the anodic reaction increases with increase in the static dielectric constant (ε) of the electrolyte. More importantly, it is found that the electron transfer rate constant (k_{et}) for the anodic reaction is directly proportional to the static dielectric constant of the ionic liquid and it can be presented as

$$\log k_{et}) = -\frac{19.265}{\varepsilon} + 0.5465 \quad (19)$$

Using the electron transfer rate constant of the electrochemical oxidation of lithium metal at the anode, the current density, i_0, can be calculated using the equation below:

$$i_0 = \frac{k_{et}\, e}{A} \quad (20)$$

where, e is the charge of an electron and A is the active surface area of the electrode. As shown in Fig. 2, the DFT calculation assumed that one out of 9 lithium atoms, located on the surface of electrode, gets oxidized and forms Li^+ ion. Therefore, the active surface area for this reaction will be the frontal area of 9 unit cells, which can be

Table 1
The boundary conditions, used in the mathematical model for Li-Air battery, are listed.

	$x = 0$	$x = L_{sp}$	$x = L_{sp} + L_{ca}$
Lithium ion concentration (C_{Li^+})	$-D_{Li,eff}\frac{\partial C_{Li^+}}{\partial x} = \frac{a i_{load}}{F}$		$\frac{\partial C_{Li^+}}{\partial x} = 0$
Oxygen concentration (C_{O_2})	$\frac{\partial C_{O_2}}{\partial x} = 0$		$C_{O_2} = s_{O2} C_{O_2,atm\,O2,atm}$
Liquid phase electric potential (ϕ_l)	$-\kappa_{eff}\frac{\partial \phi_l}{\partial x} = i_{load}$		$\frac{\partial \phi_l}{\partial x} = 0$
Solid Phase Electric Potential (ϕ_s)		$\frac{\partial \phi_s}{\partial x} = 0$	$-\sigma_{eff}\frac{\partial \phi_s}{\partial x} = i_{load}$

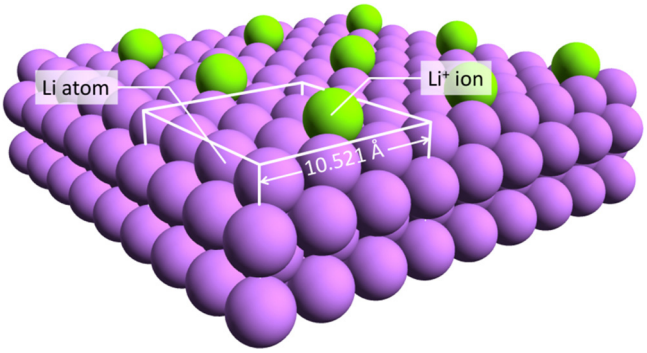

Fig. 2. The configuration of the model system used in DFT calculation of the electron transfer rate constant is shown. 9 unit cells have been shown. Pink: Neutral lithium atoms. Green: Li+ ion. (For interpretation of the references to colour in this figure legend, the reader is referred to the web version of this article.)

calculated using the lattice constant of lithium metal (3.507 Å):

$$A(m^2) = \left(3 \times 3.507 \times 10^{-10} m\right)^2 = 1.10691 \times 10^{-18} m^2$$

According to the abovementioned DFT calculations, the electron transfer rate constant for the oxidation of lithium metal in $MPPY^+TFSI^-$ ionic liquid based electrolyte, with a dielectric constant of 9.1, is 0.025082 sec^{-1}. Therefore, the exchange current density for the oxidation of metallic lithium in $MPPY^+TFSI^-$ ionic liquid is 0.363043 $\mu A/cm^2$.

3.2. Diffusivity and Solubility

We used MD simulations to evaluate Maxwell-Stephan (MS) diffusivities of the specific chemical species in the ternary systems consisting of $MPPY^+TFSI^-$ ionic liquid (IL) doped with Li^+TFSI^- as well as to calculate solubility of oxygen in the ionic liquid electrolyte. *Ab initio* calculations were performed on a cation/anion pair with the second-order Møller–Plesset (MP2) perturbation theory using the 6–31 G (d) basis set [24,25] to obtain the partial atomic charges. These calculations were performed using NWChem [26]. As described in our previous work [10], the charges were reduced to account for polarization effects. We used the software LAMMPS [27] for all classical MD simulations. All atomic interactions were described using the optimized potentials for liquid simulations (OPLS) force field [28]. Our results were validated [10] by comparing calculated properties, such as density and diffusion coefficient for neat ionic liquid and ionic liquid doped with Li^+TFSI^-, to experimental data [29]. For the doped solution (IL with Li^+TFSI^-), a mixture of 0.25 mole fraction Li^+TFSI^- with 0.75 mole fraction $MPPY^+TFSI^-$ was simulated.

3.2.1. Maxwell–Stephan Diffusivity

An *NPT* ensemble, where the number of particles (N), pressure (P), and temperature (T) are fixed, was used to equilibrate the system at atmospheric pressure and temperature of 303 K, 323 K, 343 K, 363 K and 383 K. A Nose'–Hoover barostat [30] and thermostat [31,32] were utilized to control the temperature and pressure. Production runs of *NPT* ensembles were carried out for at least 40 ns, after equilibration runs for at least 15 ns. The equations of motion were integrated with a time step of 1 fs for production runs. The cutoff distances for Coulombic and van der Waals interactions were 1.3 nm. Long range electrostatic interactions were computed using the particle–particle–particle mesh (PPPM) method [33]. The MS diffusivities were obtained from Onsager coefficients (μ) [34], which are calculated from MD simulations, using the following equation:

$$\mu_{ab} = \frac{1}{6}\lim_{n\to\infty}\frac{1}{N}\cdot\frac{1}{n\cdot\Delta t}\left\langle\left\{\sum_{i=1}^{N_a}\left[r_{i,a}(t+n\cdot\Delta t)-r_{i,a}(t)\right]\right\}\left\{\sum_{j=1}^{N_b}\left[r_{j,b}(t+n\cdot\Delta t)-r_{j,b}(t)\right]\right\}\right\rangle \quad (21)$$

Here, a and b are the types of ions, N is the total number of ions, $r_{i,a}$ denotes the position of ith ion of type a at time t. Δt is the simulation time-step, and n denotes the number of time-steps. $\langle\rangle$ denotes the ensemble average computed over n. Also, the matrix $[\mu]$ is symmetric and $\mu_{ab} = \mu_{ba}$. An approach described by Liu et al. [34] was employed to calculate the MS diffusivities presented in Table 3. Here, $D_{1,2}$ is the MS diffusivity between Li^+ and $MPPY^+$, $D_{1,3}$ between Li^+ and $TFSI^-$, and $D_{2,3}$ between $MPPY^+$ and $TFSI^-$.

As expected, the MS diffusivities between the ions are greater in magnitude at higher temperatures. Also, we observe that the MS diffusivity between Li^+- $MPPY^+$ is the lowest. This is interpreted in light of the positive charges on both the species and the repulsion between Li^+ and $MPPY^+$, which results in relatively diminished diffusion of Li^+ into $MPPY^+$. The MS diffusivities are relatively higher for Li^+- $TFSI^-$ and $MPPY^+$- $TFSI^-$ because of the opposite charges on the ion-pairs, which implicitly accounts for greater Coulombic attraction between the ion-pairs, thus resulting in increased diffusion into each other. The diffusion in Li^+- $TFSI^-$ is, however, low compared to that of $MPPY^+$- $TFSI^-$ because of the increased coordination between Li^+ and $TFSI^-$, which tend to form charged clusters. The smaller Li^+ is surrounded by multiple large $TFSI^-$ ions. This reduces the mobility of the two species and hence the MS diffusivity. Due to the similar sizes of $MPPY^+$- $TFSI^-$, cluster formation is not prevalent. Also, because of their large sizes, the surface charge densities of $MPPY^+$ and $TFSI^-$ are low. This results in relatively high mutual diffusion between the two species. The high MS diffusivity in $MPPY^+$-$TFSI^-$ can ultimately be attributed to the strong cation-anion interaction in ionic liquids [34].

3.2.2. Oxygen Solubility

We performed MD simulations to calculate the solubility of oxygen in $MPPY^+TFSI^-$ solvents, shown in Fig. 3. We used the software LAMMPS [27] for performing all MD simulations with the

same OPLS (Optimized Potentials for Liquid Systems) [35] based force field, with parameterized charges, as described earlier [10]. The configuration of the simulated domain, also described elsewhere [36], is shown in Fig. 4. The domain consisted of two sections of ionic liquid at the two ends (125 $MPPY^+$ and 125 $TFSI^-$ ions) separated from oxygen gas by a semi-permeable membrane. The membranes comprised of single layer of molecules arranged in a face centered cubic (FCC) configuration. The region between the membranes was filled with oxygen molecules. The system is periodic in all three dimensions. A Lennard-Jones potential was utilized for modeling the membrane atoms. The size parameter of this Lennard-Jones potential (σ) was adjusted to make it semi-permeable, such that only oxygen could penetrate through the membrane. The system was equilibrated as a canonical ensemble for 1,500 picoseconds at 323 K, followed by production runs involving a microcanonical ensemble, where oxygen molecules were allowed to diffuse through the membrane into the ionic liquid.

For non-ideal gases, the Henry's constant is determined from the equation [37]:

$$H_{1,2} = \frac{\varphi_1 P_1}{x_1 \exp\{P_2 V_{2\infty}/RT\}} \tag{22}$$

Here, subscript 1 refers to the solute molecules (oxygen), and 2 to the solvent molecules ($MPPY^+TFSI^-$). The pressure of the gas phase P_1 is estimated from the density of the gas phase 'ρ', the second virial coefficient of oxygen, B (cm^3/mol), gas constant, R (atm $cm^3\,K^{-1}\,mol^{-1}$), and the temperature T using the first order approximation of the virial equation of state:

$$P_1 = (1 + B\rho)\rho RT \tag{23}$$

The vapor phase fugacity coefficients φ are obtained using the equation:

$$\ln\varphi = 2\rho B - \ln\left(\frac{P}{\rho RT}\right) \tag{24}$$

The pressure in the solvent compartment P_2 is determined from the force exerted on the membranes by the solvent compartment, which provides the pressure difference between the two compartments. $V_{2\infty}$, the partial molar volume of oxygen dissolved at infinite dilution, was calculated as the difference between the volumes of two equilibrated systems with identical number of $MPPY^+TFSI^-$ ions, but with one consisting of an additional oxygen molecule. x_1 is the concentration of the solute in the solvent. The solubility (s) of oxygen in $MPPY^+TFSI^-$ can be obtained from the Henry's constant, $H_{1,2}$, using the following equation:

$$s = \frac{p}{H_{1,2}} \tag{25}$$

where p is the partial pressure of oxygen in the atmosphere.

Due to the lack of experimental data for solubility of oxygen in $MPPY^+TFSI^-$, we compared the obtained value of Henry's constant with the experimental results available for *N*-butyl-*N*-methyl pyrrolidinium bis(trifluoromethylsulfonyl) imide ($BMPY^+TFSI^-$) ionic liquid [38], which is very similar in structure to $MPPY^+TFSI$. The values of Henry's constant for the two ionic liquids are comparable within the order of magnitude. We obtained a value of 989.48 atmospheres [36] for the Henry's constant, while the reported value for $BMPY^+TFSI^-$ was 1210 ± 600 atm [38]. After qualitatively validating the results, we calculated the solubility of $MPPY^+TFSI$ in the temperature range of 303 K to 383 K at increments of 20 K. The calculated Henry's constants and corresponding oxygen solubilities are shown in Fig. 5.

Fig. 5 demonstrates that the Henry's constant decreases with increasing temperature, while the solubility of oxygen increases with temperature. Such trend in solubility, also observed for pyrrolidinium based ionic liquids[38], is explained by the lower average kinetic energy of oxygen molecules at low temperatures, which decreases the probability to overcome the solvation barrier in the ionic liquid. Thus, fewer molecules penetrate through the membrane into the ionic liquid at lower temperatures. To further verify this hypothesis, we evaluated the concentration of oxygen in the ionic liquid for identical range of temperature. Fig. 6 shows that the concentration of oxygen in the ionic liquid domain is low at 303 K and it gradually increases with increase in temperature. This implies that the oxygen density in the region between the membranes is higher at 303 K, and it gradually decreases with increase in temperature. Because of this high oxygen density, the pressure in the oxygen domain (P_1) is relatively high at 303 K, and it gradually decreases with increase in temperature. Since P_1 is directly proportional to Henry's constant, as indicated by equation (22), the Henry's constant follows the same trend as P_1 and decreases with increasing temperature.

As seen in equation (24), the fugacity (φ) plays a significant role in determining the Henry's constant. The fugacity depends on ρ, B, T and pressure P. B decreases from 14.09 cm^3/mol at 303 K to 2.49 cm^3/mol at 383 K. The density ρ decreases with increase in temperature, as explained earlier and also because x_1 increases with increase in temperature (Fig. 6). Thus the first term $2B\rho$, in equation (24), is lower at relatively higher temperatures. The second term, $ln(P/\rho RT)$, which is equivalent to $ln(1+B\rho)$, from equation (23), should decrease with increasing temperatures. However, due to the logarithmic operator, it contributes less to the overall fugacity. Therefore, the overall value of φ is dominated by the first term in equation (24) and decreases with increase in temperature. In accordance with equation (22), a decrease in the value of φ with temperature contributes to the decrease of the value of Henry's constant at higher temperatures.

Overall, the important parameters that affect the Henry's constant are φ_1, P_1 and x_1. As explained above, the results indicate

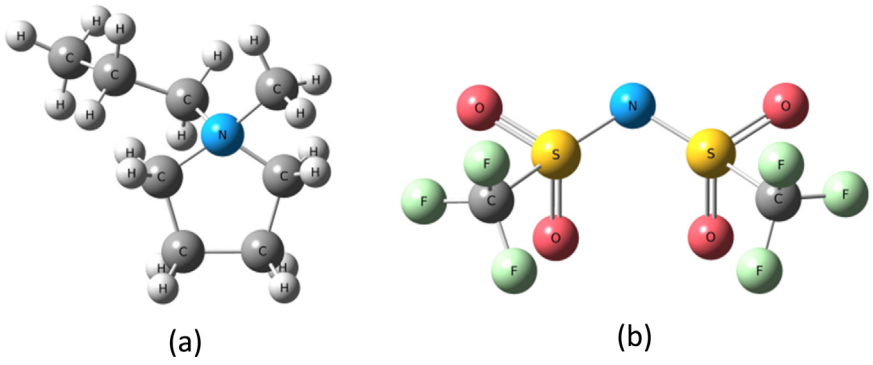

Fig. 3. Structures of (a) N-methyl-N-propylpyrrolidinium ($MPPY^+$) cation and (b) bis(trifluoromethanesulfonyl) imide ($TFSI^-$) anion are presented.

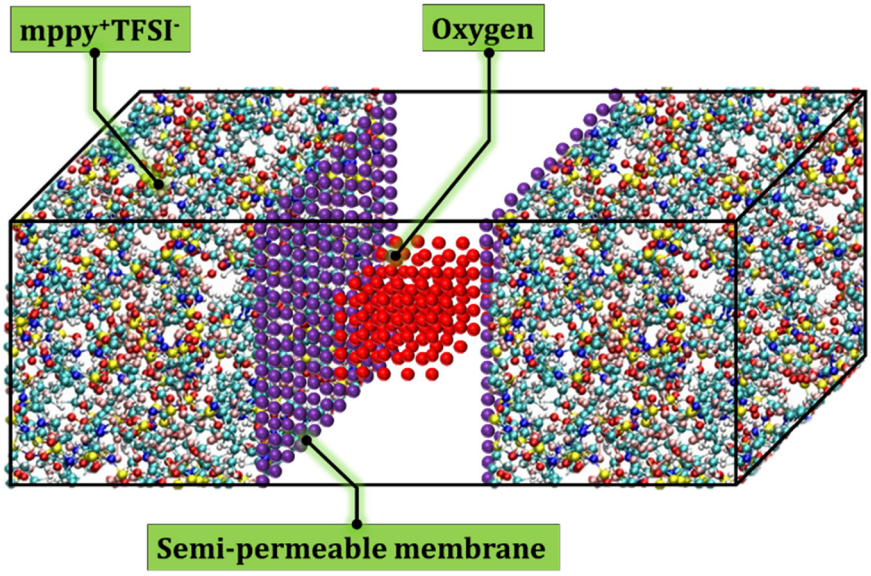

Fig. 4. Initial configuration of the simulation domain, consisting of MPPY^{+}TFSI^{-}, semi-permeable membranes and oxygen molecules, is shown.

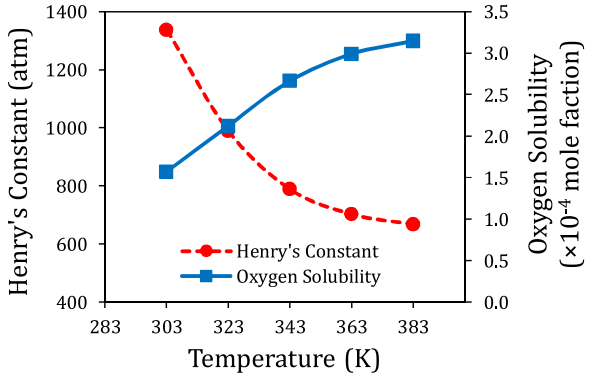

Fig. 5. The variance of Henry's constant and the solubility of oxygen (× 10,000 mole fraction) with temperature are shown. While the Henry's constant decreases with temperature, as expected, the solubility shows the opposite trend.

that φ_1 and P_1 decrease with increase in temperature and x_1 increases with increase in temperature. Therefore, despite the presence of the exponential temperature-term in the denominator of equation (22), the cumulative effect of all terms lead to decrease in Henry's constant with increase in temperature, as seen in Fig. 5. Conversely, this implies that the solubility of oxygen should increase with increase in temperature, as obtained from our simulations. The variation of x_1 with temperature gives us an overall idea about the solubility of oxygen in MPPY^{+}TFSI^{-} ionic liquid. Results obtained clearly show that the solubility of oxygen gas in MPPY^{+}TFSI^{-}, unlike other liquids, increases with increase in temperature, which can potentially improve the performance of a lithium batteries, using this ionic liquid electrolyte, at high operating temperatures. Del Sesto et al. [39] and Maton et al. [40] showed that imidazolium and pyrrolidinium-based ionic liquids do not initiate thermal decomposition until temperatures

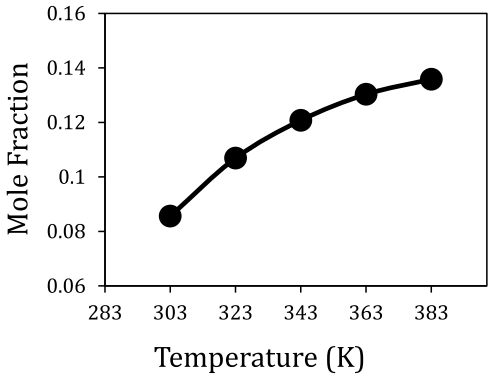

Fig. 6. The mole fraction of oxygen gas in the ionic liquid domain, x_1, is shown at various temperatures.

above 420 K. Moreover, the low vapor pressure of $MPPY^{+}TFSI^{-}$ and very high flash point [41], which makes it non-flammable, eliminates battery safety issues at high operating temperatures.

4. Results and Discussion

4.1. Model Validation

In a recent experimental study, Higashi et al. [42] presented the electrical performance of Li-air battery using ether-functionalized ionic liquid. The ionic components in their experimental work were Li+, PP13(N-methyl-N-propylpiperidinium) and TFSI(bis (trifluoromethanesulfonyl) imide). Thus, their experimental work is used to validate our model developed for the ternary electrolyte system. Here, it is assumed that diffusivity and solubility for lithium ion and oxygen remain the same in both P13 ((N-methyl-N-propylpyrrolidinium)-TFSI (our case) and PP13-TFSI (experimental work) ionic liquids since molecular structures of P13 and PP13 are very comparable. Both ionic liquids (P13TFSI and PP13TFSI) have identical methyl and propyl side chains, saturated cyclic moieties and very similar molecular weights, which should lead to comparable properties. For instance, the ionic conductivities of P13-TFSI and PP13-TFSI are 0.14 S/m and 0.15 S/m, respectively, while it is 0.22 S/m for P14-TFSI having methyl and butyl side chains [43]. Nevertheless, as shown in Fig. 7 (a), the results predicted by the numerical model are in good agreement with experiment data. Moreover, the rate capability is investigated and compared with their experiment results. To investigate rate capability, the numerical analyses are carried out on various applied current densities and the results are presented in Fig. 7 (b). The lower specific capacity limits are obtained at higher applied current densities. Table 2 shows quantitative comparison between experimental and numerical results. Due to the absence of cut-off voltage information in the experimental work, we cannot compare the rate capability of Li-air battery, quantitatively. However, it is noteworthy to mention that specific capacity limits decrease with applied current density and the specific capacity reduction trend obtained from numerical result is analogous to that obtained from experimental one. Hence, we can conclude that the developed numerical model is suitable for electrical performance evaluation of Li-air batteries that employ ionic liquid electrolytes.

4.2. Effect of Cathode Thickness

In this section, we study the effect of cathode thickness on the electrical performance of a Li-air cell. If there is no transport limitation (e.g. lithium and oxygen concentration do not change), the operating cell potential can be obtained from Tafel equations (Eqs (6a) & (6b)) as [16]

$$\phi_{cell} = E^0 - \frac{RT}{F}\ln\left(\frac{{i_{app}}^3}{F \cdot a \cdot L_{ca} \cdot C_{Li^+}^2 \cdot C_{O_2} \cdot k_c \cdot i_0^2}\right) \quad (26)$$

where E^0 is cell open circuit potential. Equation (26) is very similar to Nernst equation, where the second term in the right hand side introduces cell potential drop due to concentration polarization. This equation indicates that the voltage drop can be mitigated by increasing cathode material thickness (L_{ca}).

Fig. 8 (a) shows numerically predicted operating cell potential as a function of specific capacity for a load current density of 1 A/m^2. At very early discharge stage, operating cell potential increases with cathode thickness as is expected from Equation (26) but the cell potential decay is more severe on thicker cathode due to mass transport limitation of reaction species such as lithium ion and oxygen. Consequently lower specific capacity is obtained for thicker cathodes. For 1200 μm thick cathode case, lithium ion (Fig. 8b) and oxygen (Fig. 8c) depleted zones are found at the right and left end, respectively when specific capacity limit reaches 40 mAh/g. However, for thinner electrodes, the lithium ion and oxygen depletion zones are not noted at the same (40 mAh/g) depth of discharge (Fig. 8(b & c)). Eventually the depletion zones are observed even for thinner electrodes (400 and 800 μm) at the end of their corresponding discharge (not shown). Our numerical results, as shown in Fig. 8(d), suggest that high specific capacity can be obtained with thinner cathodes due to availability of more reaction species. For example, specific capacity limit as high as 3000 mAh/g can be obtained with a 200 μm thick cathode. Although thinner cathodes can provide better specific capacity, the cathode thickness should be optimized to maximize the cell capacity. Fig. 8(d) shows that an optimum cell capacity can be obtained for a moderate value of cathode thickness. The effect of load current density is also an important factor that influences the cell performance which is discussed later.

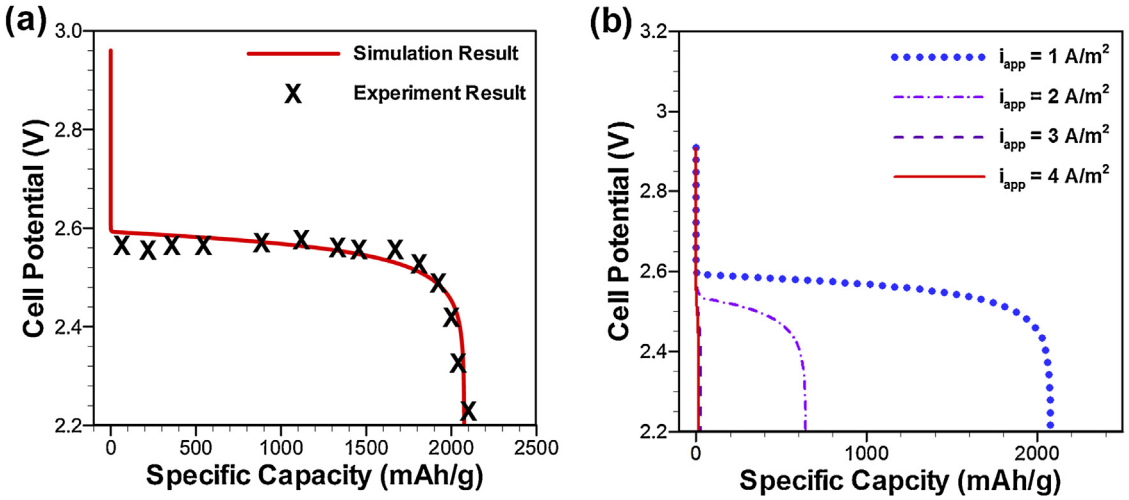

Fig. 7. (a) Electrical performance of a Li-air cell operated with ionic liquid electrolytes (P13TFSI with LiTFSI salt (0.25 mole fraction)) at 50 °C is shown for a load current density of 1 A/m^2. Experimental results of Higashi et al. [42] are also presented for comparison and model validation. Here $k_c = 2.1 \times 10^{-21}$ m^7/s-mol^2 and $a = 3.75 \times 10^{-7}$ m^{-1}. (b) Cell potential profiles are presented for various load current conditions.

Table 2
Reduction of specific capacity at different load current density conditions for room temperature ionic liquid electrolyte.

Applied load current density	Specific capacity reduction compared to the base case (Load current density of 1 A/m^2)	
	Numerical Analysis	Experiment Data
2 A/m^2	68.3%	46.6%
4 A/m^2	97.4%	93.5%

Table 3
Transport and dissolution properties, obtained from molecular dynamics (MD) simulations, are listed.

Parameter		Temperature (°C)					Unit
		30	50	70	90	110	
Maxwell-Stefan Diffusivities	D_{12}[a]	2.6625	4.1332	4.3976	10.1566	26.9723	$\times 10^{-12}$
	D_{13}[a]	4.6936	6.6999	7.5526	16.5441	44.812	(m^2/sec)
	D_{23}[a]	5.2847	8.6624	15.8614	21.352	27.7031	
Henry's constant of Oxygen		1337.35	989.48	788.61	702.56	668.01	atm
Diffusivity of Oxygen		1.213	3.416	5.412	6.732	7.526	$\times 10^{-10}$ (m^2/sec)

[a] 1: Li^+, 2: $MPPY^+$, 3: $TFSI^-$.

4.3. Effect of Operating Temperature

Previous studies indicated that solubility and diffusivity of reaction species are the key parameters to influence the performance of a Li-air battery. For instance, Read et al. demonstrated that the battery performance can be increased by increasing the oxygen solubility and diffusivity [44]. Also, Kuboki et al. [8] showed that the battery specific capacity is a strong function of electrolyte viscosity. Here, it is noteworthy that diffusivity and solubility of species are generally strong functions

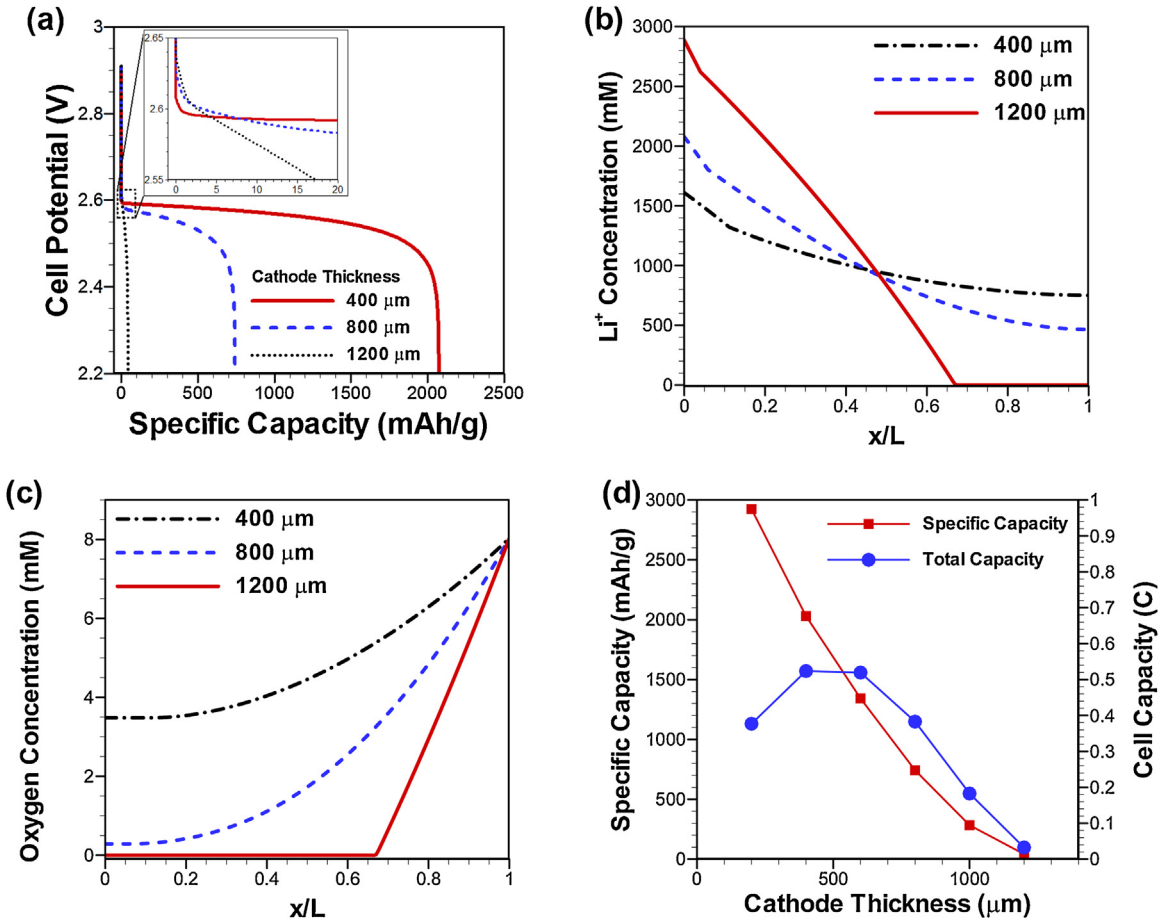

Fig. 8. Effect of cathode thickness on electrical performance of Li-air cell, operated with ionic liquid at 50 °C, is presented. (a) Cell potential profile at very early discharge stage, (b) Lithium ion and (c) oxygen concentration profile at the same discharge depth (specific capacity = 40 mAh/g) for different cathode thicknesses (400, 800 and 1200 μm) are shown. (d) Maximum specific capacity and cell capacity for various cathode thicknesses are presented.

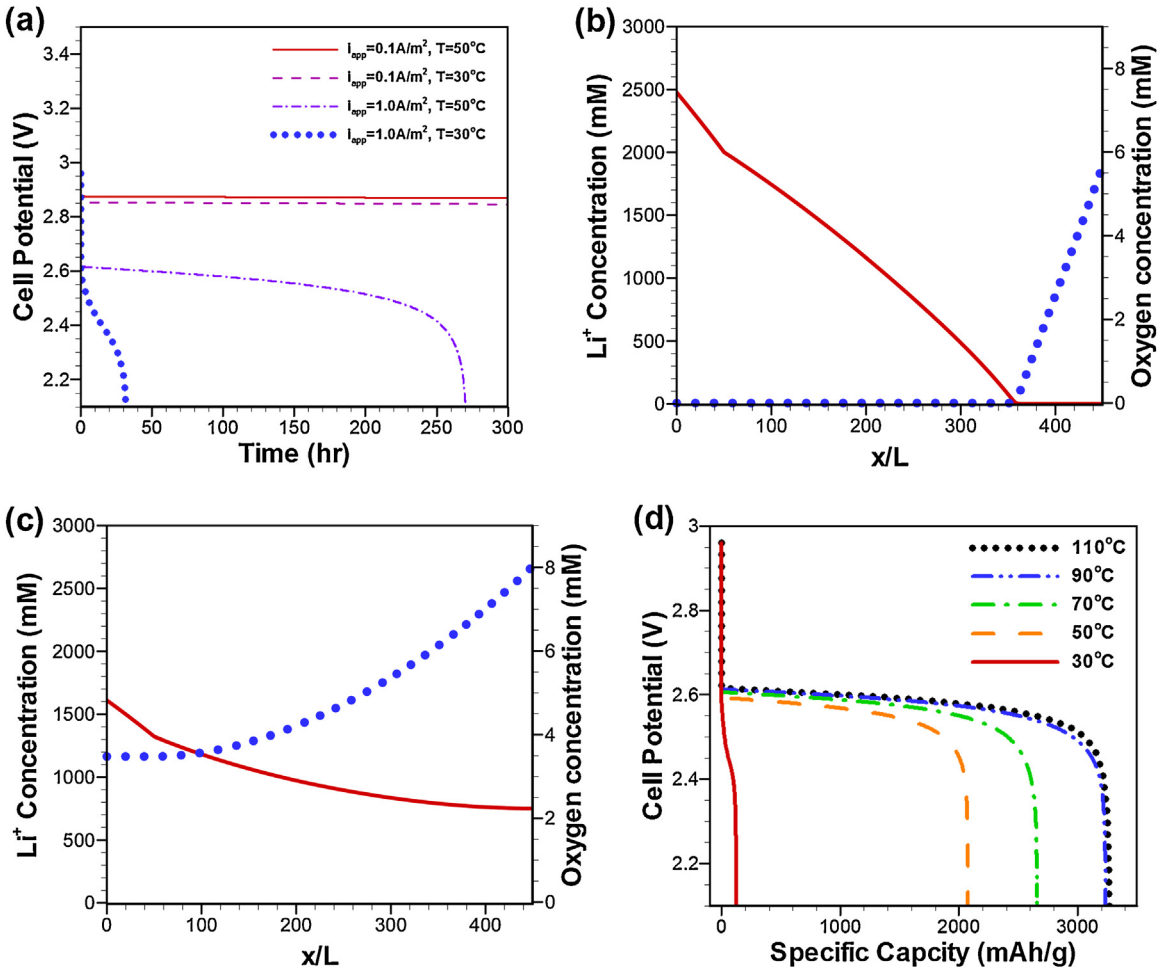

Fig. 9. Effects of cell operating temperature for Li-air battery using ionic liquid electrolytes (P13TFSI + LiTFSI salt (0.25 mole fraction)) is presented. (a) Electrical performance of a Li-air cell for various operating temperature and load current conditions is shown. Lithium ion and oxygen concentration profile at (b) 30 °C and (c) 50 °C operating temperature for the same depth of discharge (123 mAh/g). (d) Discharge cell potential profiles at different operating temperature demonstrate enhancement of maximum specific capacity with temperature.

of temperature. In a typical organic liquid electrolyte, species diffusivity increases with temperature, but oxygen solubility decreases. Therefore, at higher temperatures, the positive effect of species transport will be negated due to lower oxygen solubility. For that reason, high temperature operation of lithium battery with organic liquid does not produce any significantly different electrical performance. However, in ionic liquids, oxygen solubility is rather enhanced at higher temperatures [9]. Solubility and diffusivity of species obtained from atomistic simulations are presented in Table 3. Unlike organic electrolytes, all properties such as diffusivity and solubility modify to favorable values for battery operation at higher temperatures. Thus, it is expected that the performance will be improved by increasing operating temperature for Li-air batteries operated with ionic liquid electrolytes. It is noteworthy to mention that lithium-air batteries can be operated close to 100 °C, since ionic liquid is virtually non-flammable due to their characteristically low vapor pressures. As a matter of fact, the feasibility of battery operation at higher temperatures (e.g. 100 °C) is demonstrated experimentally by Kuboki et al. [8]. Here our objective is to study the electrical performance of Li-air battery at higher operating temperatures for different load current densities.

4.3.1. Low Load Current Density

The electrical performance of a Li-air cell is presented in Fig. 9(a) for low current density at different operating temperatures. For very low load condition (0.1 A/m^2), the electrical performance is not a strong function of operating temperature since oxygen and lithium ion transports are rarely limited. These performance results are consistent with the corresponding experimental findings [8]. However, significant improvement in the electrical performance can be obtained at higher operating temperatures for a load current density of 1.0 A/m^2 (Fig. 9(a)). For this load condition, Li-air battery suffers from oxygen and lithium ion transport limitation at room temperature. At room temperature, lithium ion and oxygen depleted zones are predicted at the end of discharge stage (depth of discharge = 123 mAh/g) (Fig. 9(b)) while, at 50 °C, the reactants are still available at the same depth of discharge stage (Fig. 9(c)) due to higher diffusivity and solubility of lithium ion and oxygen, respectively. A Li-air cell operating at 50 °C temperature will eventually face the reactant depleted regime due to pore blocking at the end of its specific capacity limit. The depletion of lithium ion and oxygen is delayed even further at higher temperatures (above 50 °C operating temperature) for a load current density of 1.0 A/m^2 (Fig. 9(d)) since higher operating temperatures result in higher solubility and diffusivity. At 110 °C

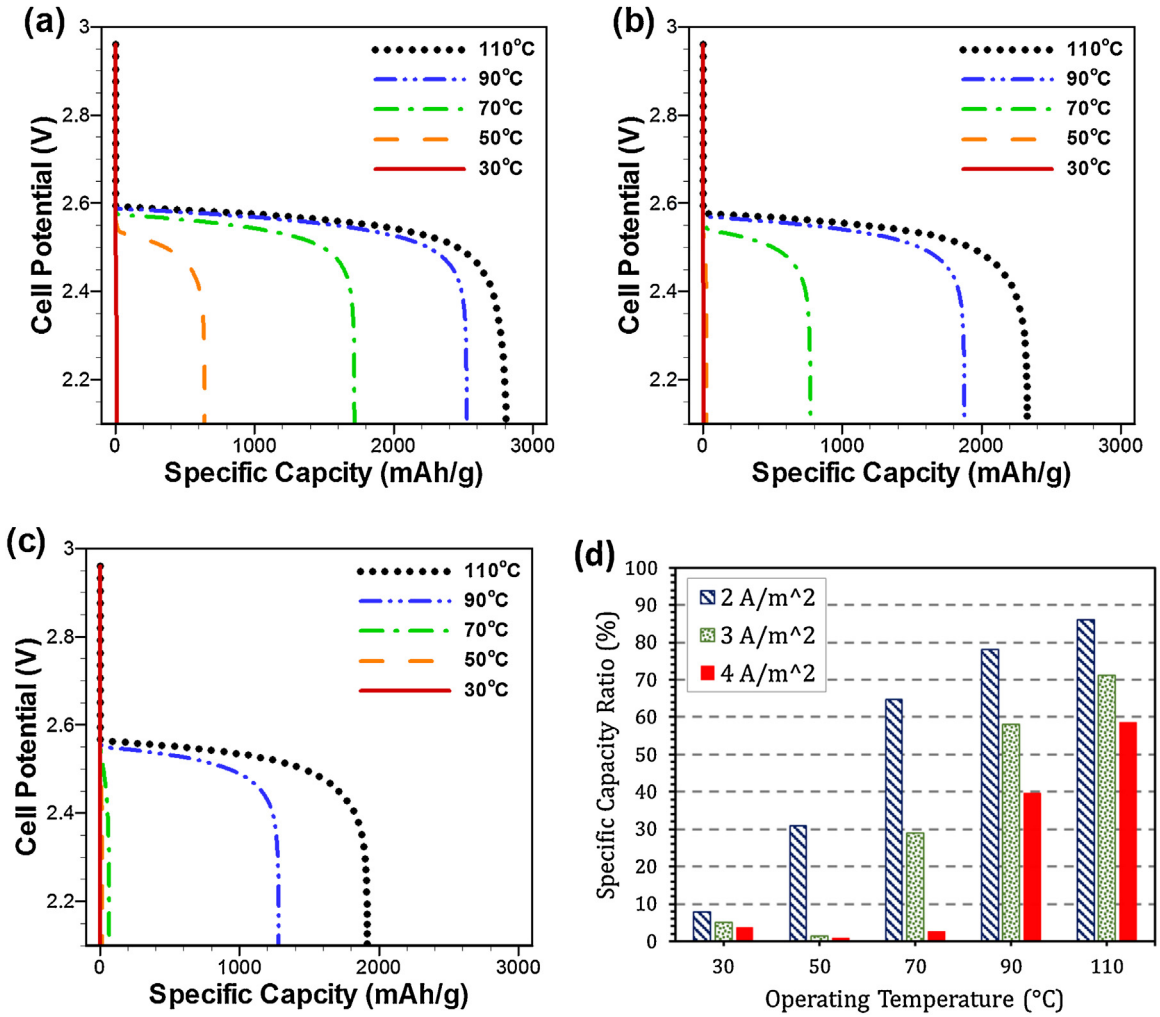

Fig. 10. Rate Capability improvement is observed with increase in operating temperature. Electrical performance of a Li-air cell during discharge is presented for an applied load current density of (a) 2 A/m^2 (b) 3 A/m^2 (c) 4 A/m^2. (d) Maximum specific capacity ratio with respect to maximum specific capacity at 1 A/m^2 for various load current conditions is shown.

operating temperature, the cell specific capacity is 26 times higher than that of room temperature operation (30 °C).

4.3.2. High Load Current Density

As discussed earlier, the cell potential drops severely with high applied current density since the battery suffers significantly from reactant species limitation at such operating conditions. Due to this reason, in most Li-air cell studies, the operating current density is kept relatively low and it is one of the main drawbacks of Li-air battery. This poor rate capability of lithium-air cell is the major bottleneck towards commercial dominance of this technology [45]. However, the limitations of lithium ion and oxygen can be alleviated by increasing operating temperature so that the problem of poor rate capability can be ameliorated. Figs. 10(a), (b) and (c) show cell performance profile for load current densities of 2, 3 and 4 A/m^2, respectively. For 50 °C operating temperature, the cell specific capacity decreased to 642 mAh/g from 2200 mAh/g as load current is increased to 2 A/m^2 from 1 A/m^2. The specific capacity decreases further (30 mAh/g and 16 mAh/g) for 3 A/m^2 and 4 A/m^2 load condition at 50 °C operating temperature. However, for all load current densities, the specific capacity improves with the operating temperature. Fig. 10(d) shows specific capacity ratio for different load current conditions, where the performance results of 1 A/m^2 load condition is used as the base case. At higher temperatures, the rate capability improvement is possible, even for severe load conditions. For instance, at 4 A/m^2 load current density, the rate capability of the Li-air cell will be 58% of that for 1 A/m^2 load condition at 110 °C, while it is only 2% for a cell operated at 70 °C. Therefore, we can circumvent poor rate capability problems in Li-air battery to a great extent by increasing operating temperature due to unusual favorable characteristics of ionic liquid electrolytes at higher operating temperatures.

4.3.3. Optimization of Cathode Thickness

In a recent experimental study, Higashi et al. [42] investigated the electrical performance of ionic liquid based Li-air cell at reasonable (1.0 A/m^2) load current condition. However, in their work, the cell was operated with a very thin cathode (80 μm) compared to most Li-air batteries (more than 200 μm [4,14]). The thickness of cathode is very important in estimating the overall cell capacity. Although transport limitation can be avoided (or delayed) with thinner electrodes, the cell capacity also suffers in thinner cathode cells. Our study reveals that the battery capacity could be improved with operating temperature due to oxygen solubility and species diffusivity enhancements. Fig. 11 shows cell capacity of a 1×1 cm^2 cell for different cathode thicknesses and operating temperatures. These predicted cell capacity profiles indicate that there is an optimum cell thickness for an operating temperature. For example, at 50 °C operating condition, one can obtain 0.53 C capacity with a 400 μm thick cathode. Any other cathode thickness

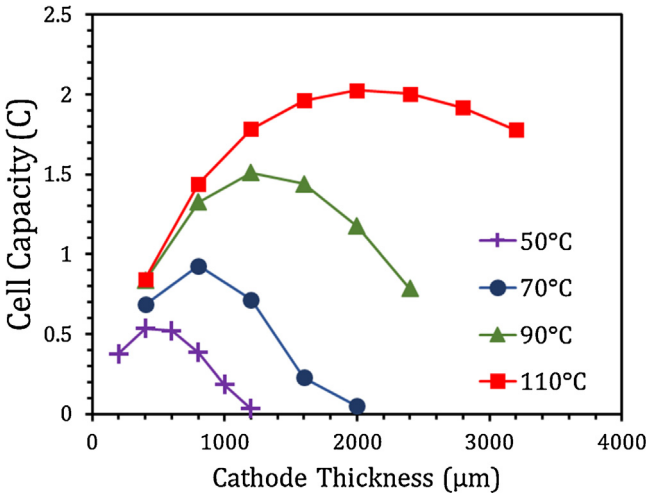

Fig. 11. Predicted cell capacities for various cathode thicknesses at different operating temperatures are presented.

will provide decreased cell capacity at 50 °C. For thinner cathodes, cell capacity will be lower due to less cathode volume even if one can obtain higher specific capacity, and vice versa for thicker cathode. The optimum cathode thickness also increases with temperature resulting in higher cell capacity. For example, one can obtain 2.0 C cell capacity with 2,000 μm thick cathode at 110 °C operating temperature, which is almost 4 times higher than that at 50 °C.

5. Conclusions

In this study, a mathematical model for Li-air battery is developed for ionic liquid based ternary electrolytes. A new species transport equation is formulated for lithium ion in the form of Nernst–Planck equation by introducing apparent diffusivity and mobility. Moreover, governing equation for liquid phase electric potential was formulated and ionic conductivity was obtained in terms of Maxwell–Stefan diffusivity and concentration. To verify our mathematical model for the Li-air cell, the electrical performance calculated from the numerical simulation is compared to experimental results. The specific capacity limit and operating potential predicted from numerical model are in good agreement with experimental values for identical operating conditions. After adequately validating the numerical model, the performances of Li-air cells operated with ionic liquid electrolyte are predicted at higher operating temperatures. Here, all electrochemical properties for the continuum based numerical model, such as solubility, diffusivity and reaction rate constant, are obtained from MD simulations and DFT calculations. Atomistic calculations reveal that transport properties, such as lithium ion diffusivity and oxygen solubility, are affected favorably in ionic liquid electrolytes at higher operating temperatures. This fact is in direct contrast with that in commonly used organic electrolytes, where the oxygen solubility decreases with temperature. Our model predicts that higher operating temperature improves electrical performance of ionic liquid based Li-air cell due to these favorable properties. Also, rate capability, which is very poor in organic electrolyte based Li-air batteries, can be improved significantly in ionic liquid based Li-air batteries operated at elevated temperatures. We also predicted the optimum cathode thickness for different working temperatures of an ionic liquid based Li-air battery. For a constant load current density, the optimal cathode thickness increases with temperature. Considering the very low vapor pressures of ionic liquids, it is possible to operate a Li-air cell with ionic liquid electrolyte at high temperatures (as high as 110 °C) to achieve significantly improved cell performances.

Acknowledgments

This work was supported in part by the Washington State Joint Center for Aerospace Technology Innovation (JCATI) grant.

References

[1] C.C. Chan, The state of the art of electric, hybrid, and fuel cell vehicles, Proceedings of the Ieee 95 (2007) 704–718.
[2] G. Girishkumar, B. McCloskey, A.C. Luntz, S. Swanson, W. Wilcke, Lithium – air battery: Promise and challenges, Journal of Physical Chemistry Letters 1 (2010) 2193–2203.
[3] M. Wakihara, Recent developments in lithium ion batteries, Materials Science & Engineering: R 33 (2001) 109–134.
[4] S.D. Beattie, D.M. Manolescu, S.L. Blair, High-Capacity Lithium-Air cathodes, Journal of the Electrochemical Society 156 (2009) A44–A47.
[5] J. Xiao, D. Mei, X. Li, W. Xu, D. Wang, G.L. Graff, W.D. Bennett, Z. Nie, L.V. Saraf, I. A. Aksay, J. Liu, J.-G. Zhang, Hierarchically porous graphene as a lithium-air battery electrode, Nano Letters 11 (2011) 5071–5078.
[6] H.-G. Jung, J. Hassoun, J.-B. Park, Y.-K. Sun, B. Scrosati, An improved high-performance lithium-air battery, Nature Chemistry 4 (2012) 579–585.
[7] D. Guyomard, J.M. Tarascon, High-voltage stable liquid electrolytes for Li1 + xMn2O4/carbon rocking-chair lithium batteries, Journal of Power Sources 54 (1995) 92–98.
[8] T. Kuboki, T. Okuyama, T. Ohsaki, N. Takami, Lithium-air batteries using hydrophobic room temperature ionic liquid electrolyte, Journal of Power Sources 146 (2005) 766–769.
[9] J.L. Anthony, J.L. Anderson, E.J. Maginn, J.F. Brennecke, Anion effects on gas solubility in ionic liquids, Journal of Physical Chemistry B 109 (2005) 6366–6374.
[10] A. Deshpande, L. Kariyawasam, P. Dutta, S. Banerjee, Enhancement of Lithium Ion Mobility in Ionic Liquid Electrolytes in Presence of Additives, Journal of Physical Chemistry C 117 (2013) 25343–25351.
[11] P.G. Bruce, S.A. Freunberger, L.J. Hardwick, J.M. Tarascon, Li-O-2 and Li-S batteries with high energy storage, Nature Materials 11 (2012) 19–29.
[12] M. Doyle, Modeling of galvanostatic charge and discharge of the lithium/polymer/insertion cell, J. Electrochem. Soc. Journal of The Electrochemical Society 140 (1993).
[13] P. Albertus, G. Girishkumar, B. McCloskey, R.S. Sanchez-Carrera, B. Kozinsky, J. Christensen, A.C. Luntz, Identifying capacity limitations in the li/oxygen battery using experiments and modeling, Journal of the Electrochemical Society 158 (2011) A343–A351.
[14] U. Sahapatsombut, H. Cheng, K. Scott, Modelling the micro-macro homogeneous cycling behaviour of a lithium-air battery, Journal of Power Sources 227 (2013) 243–253.
[15] K. Yoo, S. Banerjee, P. Dutta, Modeling of volume change phenomena in a Li-air battery, Journal of Power Sources 258 (2014) 340–350.
[16] K. Yoo, A. Deshpande, S. Banerjee, P. Dutta, Electrochemical model for ionic liquid electrolytes in lithium batteries, Electrochimica Acta 176 (2015) 301–310.
[17] D.A.G. Bruggeman, Berechnung verschiedener physikalischer Konstanten von hetarogenen Substanzen, Ann. Physik 24 (1935) 636–679.

[18] D.-W. Chung, M. Ebner, D.R. Ely, V. Wood, R.E. Garcia, Validity of the Bruggeman relation for porous electrodes, Modelling and Simulation in Materials Science and Engineering 21 (2013).
[19] T.R. Ferguson, M.Z. Bazant, Nonequilibrium Thermodynamics of Porous Electrodes, Journal of the Electrochemical Society 159 (2012) A1967–A1985.
[20] R.A. Marcus, Electron-transfer reactions in chemistry – theory and experiment, Reviews of Modern Physics 65 (1993) 599–610.
[21] A. Klamt, G. Schuurmann, COSMO: a new approach to dielectric screening in solvents with explicit expressions for the screening energy and its gradient, Journal of the Chemical Society, Perkin Transactions 2 (1993) 799–805.
[22] S. Kazemiabnavi, P. Dutta, S. Banerjee, Density functional theory based study of the electron transfer reaction at the lithium metal anode in a lithium–air battery with ionic liquid electrolytes, The Journal of Physical Chemistry C 118 (2014) 27183–27192.
[23] S. Kazemiabnavi, P. Dutta, S. Banerjee, A density functional theory based study of the electron transfer reaction at the cathode-electrolyte interface in lithium-air batteries, Physical Chemistry Chemical Physics 17 (2015) 11740–11751.
[24] R. Ditchfield, W.J. Hehre, J.A. Pople, Self-consistent molecular orbital methods. 9. Extended gaussian-type basis for molecular-orbital studies of organic molecules, J. Chem. Phys. 54 (1971).
[25] W.J. Hehre, R. Ditchfield, J.A. Pople, Self-consistent molecular orbital methods. 12. Further extensions of gaussian-type basis sets for use in molecular-orbital studies of organic-molecules, Journal of Chemical Physics 56 (1972).
[26] M. Valiev, E.J. Bylaska, N. Govind, K. Kowalski, T.P. Straatsma, H.J.J. Van Dam, D. Wang, J. Nieplocha, E. Apra, T.L. Windus, W.A. de Jong, NWChem: A comprehensive and scalable open-source solution for large scale molecular simulations, Computer Physics Communications 181 (2010) 1477–1489.
[27] S. Plimpton, Fast parallel algorithms for short-range molecular-dynamics, Journal of Computational Physics 117 (1995) 1–19.
[28] E.K. Watkins, W.L. Jorgensen, Perfluoroalkanes: Conformational analysis and liquid-state properties from ab initio and Monte Carlo calculations, Journal of Physical Chemistry A 105 (2001) 4118–4125.
[29] I. Nicotera, C. Oliviero, W.A. Henderson, G.B. Appetecchi, S. Passerini, NMR investigation of ionic liquid-LiX mixtures: Pyrrolidinium cations and TFSI-anions, Journal of Physical Chemistry B 109 (2005) 22814–22819.
[30] G.J. Martyna, D.J. Tobias, M.L. Klein, Constant-pressure molecular-dynamics algorithms, Journal of Chemical Physics 101 (1994) 4177–4189.
[31] S. Nose, M.L. Klein, Constant pressure molecular-dynamics for molecular-systems, Molecular Physics 50 (1983) 1055–1076.
[32] W.G. Hoover, Canonical dynamics – equilibrium phase-space distributions, Physical Review A 31 (1985) 1695–1697.
[33] J.W. Eastwood, R.W. Hockney, D.N. Lawrence, P3M3DP – The 3-dimensional periodic particle-particle-particle-mesh program, Computer Physics Communications 19 (1980) 215–261.
[34] X. Liu, T.J.H. Vlugt, A. Bardow, Maxwell-Stefan diffusivities in binary mixtures of ionic liquids with dimethyl sulfoxide (DMSO) and H2O, Journal of Physical Chemistry B 115 (2011) 8506–8517.
[35] W.L. Jorgensen, D.S. Maxwell, J. TiradoRives, Development and testing of the OPLS all-atom force field on conformational energetics and properties of organic liquids, Journal of the American Chemical Society 118 (1996) 11225–11236.
[36] A. Deshpande, P. Dutta, S. Banerjee, Solubility of oxygen in lithium-air battery electrolytes: a molecular dynamics study, Proceedings of the ASME IMECE 2014, Montreal, Canada, 2014.
[37] M. Krishnamurthy, S. Murad, J.D. Olson, Molecular dynamics simulation of Henry's constant of argon nitrogen, methane and oxygen in ethylene oxide, Molecular Simulation 32 (2006) 11–16.
[38] J.L. Anthony, J.L. Anderson, E.J. Maginn, J.F. Brennecke, Anion Effects on Gas Solubility in Ionic Liquids, The Journal of Physical Chemistry B 109 (2005) 6366–6374.
[39] R.E. Del Sesto, T.M. McCleskey, C. Macomber, K.C. Ott, A.T. Koppisch, G.A. Baker, A.K. Burrell, Limited thermal stability of imidazolium and pyrrolidinium ionic liquids, Thermochimica Acta 491 (2009) 118–120.
[40] C. Maton, N. De Vos, C.V. Stevens, Ionic liquid thermal stabilities: decomposition mechanisms and analysis tools, Chemical Society Reviews 42 (2013) 5963–5977.
[41] H.-J. Liaw, C.-C. Chen, Y.-C. Chen, J.-R. Chen, S.-K. Huang, S.-N. Liu, Relationship between flash point of ionic liquids and their thermal decomposition, Green Chemistry 14 (2012) 2001–2008.
[42] S. Higashi, Y. Kato, K. Takechi, H. Nakamoto, F. Mizuno, H. Nishikoori, H. Iba, T. Asaoka, Evaluation and analysis of Li-air battery using ether-functionalized ionic liquid, Journal of Power Sources 240 (2013) 14–17.
[43] K. Hayamizu, Y. Aihara, H. Nakagawa, T. Nukuda, W.S. Price, Ionic conduction and ion diffusion in binary room-temperature ionic liquids composed of emim BF4 and LiBF4, Journal of Physical Chemistry B 108 (2004) 19527–19532.
[44] J. Read, K. Mutolo, M. Ervin, W. Behl, J. Wolfenstine, A. Driedger, D. Foster, Oxygen transport properties of organic electrolytes and performance of lithium/oxygen battery, Journal of the Electrochemical Society 150 (2003) A1351–A1356.
[45] M. Armand, J.M. Tarascon, Building better batteries, Nature 451 (2008) 652–657.